nature nanotechnology

SUPPLEMENTARY INFORMATION

DOI: 10.1038/NNANO.2015.160

High-frequency nano-optomechanical disk resonators in liquids

E. Gil-Santos, C. Baker, D. T. Nguyen, W. Hease, C. Gomez, A. Lemaître, S. Ducci, G. Leo and I. Favero

1. Optomechanical measurements with and without thermal contributions

The results presented in the main text have been obtained on GaAs disk resonators. These resonators present some level of residual optical absorption at their surface. The amplitude of surface absorption varies from one semiconductor material to another, and also depends on specific surface treatments. In the low optical power limit, surface absorption does not impact experimental results but at large power and with the high optical Q at play, it results in a local heating, with optical and mechanical consequences that need to be controlled. Supplementary Fig. 1a shows for example optical spectra acquired on a 3μm radius GaAs disk in a liquid at low and high optical power. At low power, the symmetric Lorentzian optical resonance indicates a linear behavior of the disk optical mode, with no heating. The loaded optical Q is $1.4 \cdot 10^4$, with an important contribution of radiation (bending) losses (this point is clarified in Supplementary Fig. 2 below). At high optical power, we observe a distortion of the optical resonance, which is a signature of heating [1,2]. Fabry-Perot interferences are observed in both spectra: they are produced by light refraction at both ends of the waveguide, and can be suppressed in specifically engineered structures. The thermal distortion of optical resonances in GaAs disks is known to result from the thermo-optic effect, with little role played by thermal expansion of the disk. The temperature increase in the disk ΔT corresponding to an optical resonance shift $\Delta\lambda$ is $\Delta T = n(\Delta\lambda/\lambda)/(dn/dT)$ with n the refractive index[3]. At the highest optical power attainable in our experiments, the wavelength shift approaches 4 nm, corresponding to ΔT of about 50K. As the mechanical properties of both GaAs and the liquid change with temperature, the high optical power regime can lead to changes in the measured mechanical resonance frequency and quality factor.

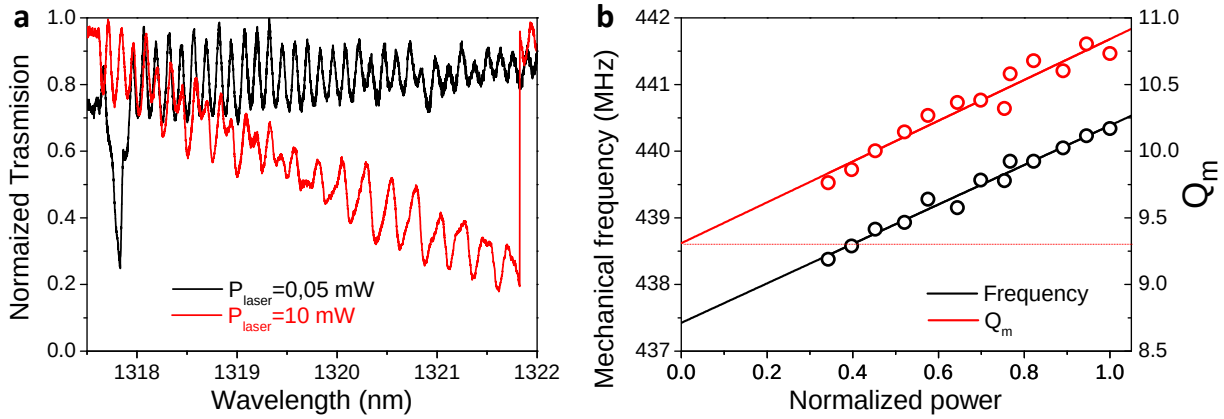

Supplementary Figure 1: Control of optomechanical thermal effects at large optical power. a, Optical spectra of a 3 μm radius disk at low and high laser power (factor 20 difference), with (arbitrary) power level indicated by the laser controller 0.05 mW (black) and 10 mW (red). **b,** Mechanical resonance frequency (black) and mechanical quality factor (red) as a function of the normalized optical power circulating in the disk. Open circles are measurements while solid lines are linear fits. The symbol size is the experimental error bar. As the power is increased, the heating of the surrounding liquid results in a reduction in both its viscosity and density. This in turn results in an increase in both Q_m and mechanical frequency. The extrapolation of the mechanical resonance frequency and quality factor at zero power allows us to measure the mechanical properties of the resonator at room temperature (the red dashed line is a guide to the eye for the extrapolation of Q_m at zero power).

Regarding the mechanical properties of the resonator in the liquid, two effects must be accounted for. On one hand, a temperature increase reduces the Young's modulus of GaAs, making the disk 'softer' and lowering its mechanical resonance frequency. On the other hand, as the liquid's temperature also increases, its viscosity and density are lowered, leading to a diminution of the dissipated energy and added mass. This in turn tends to raise both the mechanical quality factor and frequency. As shown in Supplementary Fig. 1b, the thermal effects on the liquid are dominant in experimental observations, and a linear increase in the frequency and quality factor is measured as a function of optical power. The temperature elevation in the disk evolves linearly with the dropped power, while the liquid's viscosity and density decrease linearly as the temperature rises. Overall, the summed contributions produce a linear

behavior for both the frequency and quality factor as a function of optical power. This linear behavior allows the extrapolation of measured quantities down to zero optical power, enabling a precise estimation of frequency and Q.

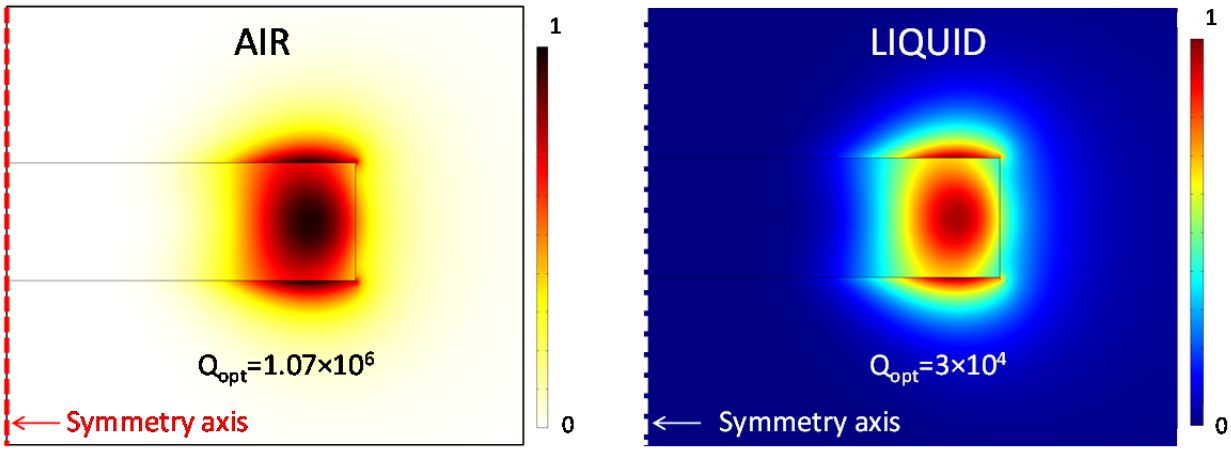

Supplementary Figure 2: Change in radiative optical Q upon immersion. FEM simulation of the whispering gallery mode employed in experiments on a 1 μm radius GaAs disk of thickness 320 nm (WGM TM-polarized, p=1,m=10), performed both when the disk is surrounded by air (left panel) and when the disk is immersed in a liquid (right panel). The color scale indicates the normalized modulus of the electric field. The three perfluorinated liquids employed in our experiments have similar refractive index n=1.24, a value larger than air refraction, which leads to a reduction of the radiative optical Q from 1.7×10^6 to 30 000. In experiments, depending on the exact guide/disk optical coupling, the measured loaded Q is always smaller than this radiative limit value. The fact that the optical Q measured in liquid (Q=22 000, see Main Text) approaches the radiative value is indicative of the fact that bending losses are the dominating source of optical dissipation when a disk of radius 1 micron is operated in liquid.

2. Analytical model of the RBM mode profile

Following Love's theory for the rotation-invariant radial extension of a circular plate, we obtain the following expression for the radial displacement Ψ_r at any point r of a plate of radius R with free boundary conditions [4,5]:

$$\Psi_r(r) = A_p \cdot J_1(\lambda_p r/R) \quad \text{(S1)}$$

where r is the distance to the symmetry axis of the disk (Supplementary Fig. 3a), J_n the n^{th} order Bessel function of the first kind, A_p a normalization constant. λ_p (the frequency-parameters) are solutions of the equation $\lambda_p J_0(\lambda_p)-(1-\nu)J_1(\lambda_p)=0$ and are linked to the mechanical frequencies through $\omega_p = \frac{\lambda_p}{R}\sqrt{\frac{E}{\rho_s(1-\nu^2)}}$, where p is the radial order of the considered radial extensional mode (RBM). ν, E and ρ_s are respectively the Poisson ratio, Young's modulus and density of the plate material. This plate model neglects the out-of-plane displacement along the z-axis, but it provides accurate analytical expressions for the mechanical resonance frequency and for the radial displacement of a disk's RBM. The z-displacement can be obtained by following Love's work[4] on longitudinal vibrations of circular cylinders and imposing a linear dependence of the out of plane displacement Ψ_z with z, the distance to the neutral plane of the disk plate (Supplementary Fig. 3a). We finally obtain

$$\Psi_z(r,z) = A_p \cdot \frac{\frac{1-\nu}{\nu} J_1'(\lambda_p \cdot r/R)\big|_{r=R} + J_1(\lambda_p)/R}{J_0(\lambda_p)} \cdot J_0(\lambda_p \cdot r/R) \cdot z \quad \text{(S2)}$$

To verify this model and its ability to accurately describe both radial and out-of-plane displacements, we compare the outcomes of (S1) and (S2) with 2D axi-symmetric FEM simulations. Supplementary Fig. 3b

and c show an excellent level of agreement between our analytical elastic theory and FEM simulations for disks of varying thickness and radius. The agreement improves as the radius to thickness ratio increases.

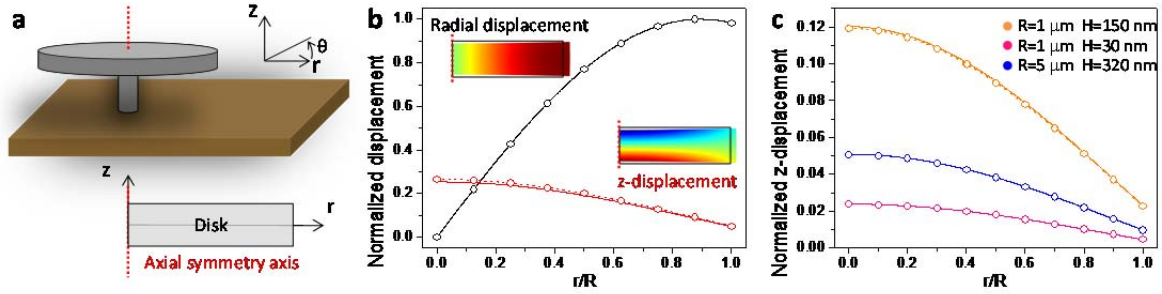

Supplementary Figure 3: Analytical elastic model of a RBM. a, Top: 3D schematic of a GaAs disk sitting on its pedestal. Bottom: Simplified 2D representation of a GaAs disk by a circular plate (without pedestal) with axial symmetry along z. **b,** Comparison between FEM simulations (symbol and dashed line) and analytical model (solid line), for the normalized radial (resp out-of-plane) displacement amplitude $\boldsymbol{\psi_r/\psi_r^{max}}$ (**resp** $\boldsymbol{\psi_z/\psi_r^{max}}$) in black (resp in red) as a function of the normalized radial position r/R. The comparison is made for the first order (p=1) RBM of a GaAs disk with 1 μm radius and 320 nm thickness. The insets show the radial and z-displacements in color scale. **c,** Same comparison for the normalized out-of-plane displacement for 3 distinct disks of radius R and thickness H.

3. FEM simulations

The interaction between the disk resonator and the surrounding liquid is analyzed using the Finite Element Method (FEM). Simulations are carried out in 2D (r,z plane), taking advantage of the axial symmetry of the disk. We compute the viscous and the acoustic interactions separately, as was done for the analytical model.

The viscous regime simulations are performed in the time domain. The speed of sound in the liquid is taken to be infinite and the bulk viscosity (friction in the longitudinal liquid motion) equal to zero. A normal static force is applied onto the disk sidewall and relaxed at time zero. We then compute the time evolution of the sidewall's displacement amplitude. The amplitude oscillates at a frequency matching the first order RBM and its envelope decays exponentially as shown in Supplementary Fig. 4a. The disk is considered alone, without pedestal, and is placed 2 μm above the substrate's surface, as in experiments (Supplementary Fig. 4b). We use two complementary methods to extract the quality factor from the time trace. First, we perform a Fast Fourier Transform of the displacement and fit the resonant peak of interest to a Lorentzian peak. We obtain this way the angular resonance frequency ω and the Full Width at Half Maximum (FWHM), leading to $Q = \omega/FWHM$. Second, we filter the signal using a band pass around the RBM frequency of interest and select the time-dependent amplitude extrema in order to fit them by exponential decays of the form $A(t) = A_0 \cdot e^{-t/\tau}$. The time decay constant τ and the resonant frequency f directly give the quality factor $Q = \pi\tau f$. Both methods agree within 1% for disks investigated here. This comparison between the time-domain and frequency-response methods was also carried-out in the case of a commercial cantilever in the viscous regime. Using the two methods in parallel minimizes the risk of misinterpretation caused by the coupling between different mechanical modes. This difficulty induced by mode-coupling convinced us to study simple disks without pedestal. Even if the simulations are also meaningful when taking the pedestal into account, an exhaustive analysis of eigenmodes must be done in first place. In addition, the Q factor obtained for the disk-pedestal is in good agreement with that of the isolated disk as the pedestal radius is reduced to small values like in our experiments.

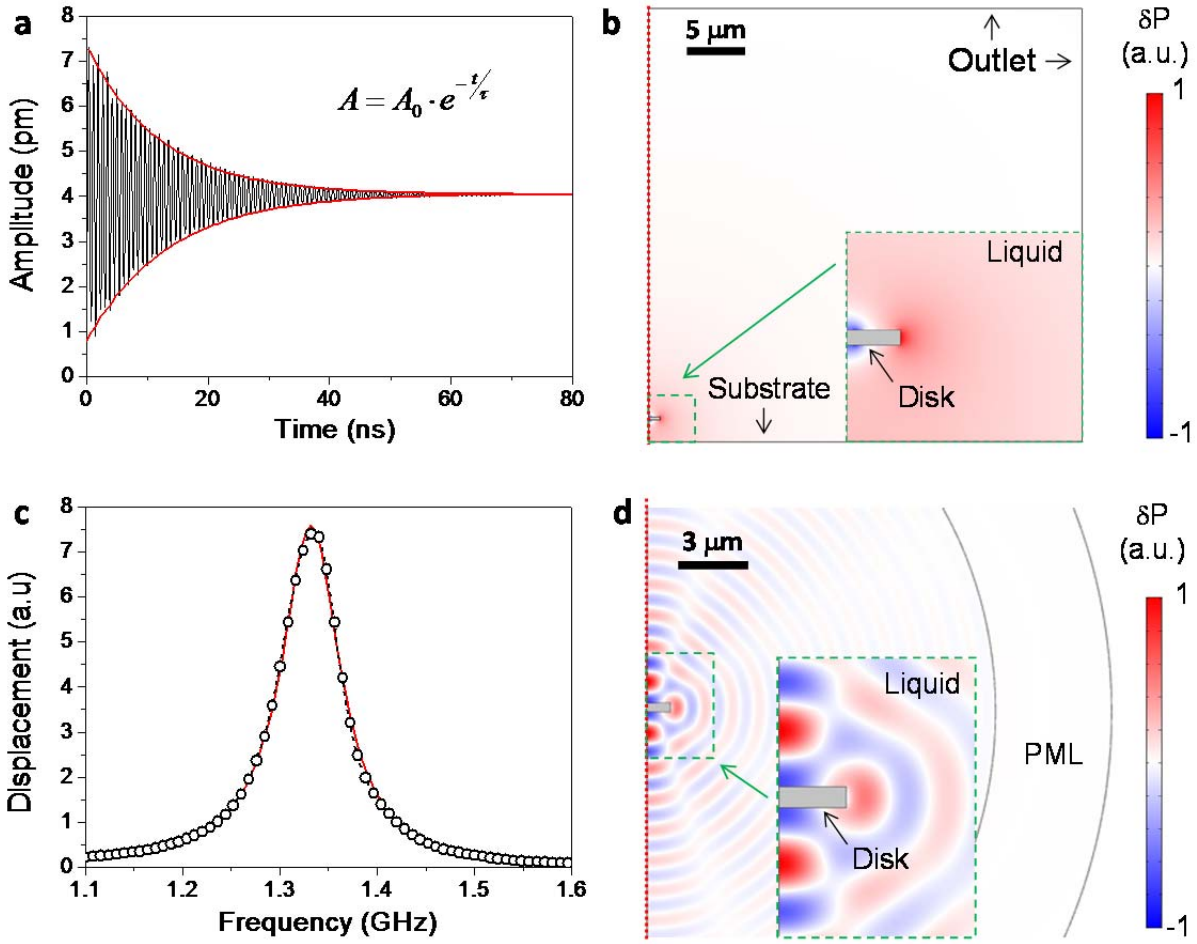

Supplementary Figure 4: FEM simulations in the viscous and acoustic regimes for a disk with R=1 μm and H=320 nm. a, Viscous regime. Time evolution of the disk sidewall's displacement's amplitude (black), after relaxing a 1 μN radial force applied on the sidewall. Exponential fits (red) of the amplitude's extrema used to estimate the mechanical Q. **b,** Viscous regime. Pressure variation field in the liquid, in response to the disk motion, pictured at time t= 0.84 ns. The image illustrates the chosen boundary conditions (axial symmetry, substrate, outlets on the top and right edges). A no-slip condition is imposed on the substrate boundary, while a condition of fixed pressure in absence of viscous stress was imposed on the top and right external boundaries. The inset is a close-up of the disk's vicinity where pressure variations are considerably larger. **c,** Acoustic regime. Frequency response of the disk to an applied time dependent radial force of 1 μN exerted at the sidewall (black dash line and symbols). The Lorentzian fit (red line) is used to extract the mechanical quality factor and the frequency shift produced by acoustic interactions. **d,** Acoustic regime. Pressure variations in the liquid associated with the motion of the disk at the

resonance frequency of 1.33 GHz. The perfectly match layer (PML) that prevents reflection of the acoustic waves is shown for clarity. The inset is a close-up of the disk's vicinity revealing the complexity of the pressure field and the importance of interference effects. Note that in the acoustic regime, pressure waves propagate to large distances in contrast to the viscous regime.

Note that viscous dissipation occurs in the vicinity of the disks and decays quickly with the distance to the disk, as exemplified by the highly localized pressure gradients visible in Supplementary Fig. 4b. With this in mind, there are several constraints in the numerical parameters. The computation volume must be large enough to avoid reflections of pressure waves on its boundaries. At the same time, the mesh in the disk's vicinity must be very fine with element sizes on the order of nanometers. Moreover the time steps, typically 100 times smaller than the mechanical period, must lie in the few picoseconds range while the total decay time can reach hundreds of nanoseconds, depending on the quality factor. Numerical convergence has been checked carefully with all parameters. As a consequence of these requirements, one such 2D simulation takes about half a day on a powerful personal computer, thereby underlining the appeal of analytical models.

FEM simulations in the acoustic regime are performed in the frequency domain. In this regime, the standard viscosity (shear viscosity) and the bulk viscosity (longitudinal) are zero but the liquid becomes compressible in the volume and possesses a finite Bulk elastic modulus. Again a radial force is applied on the sidewall of the disk, but it is now modulated in time. By sweeping the modulation frequency around the first order RBM frequency, the displacement's amplitude response is obtained like shown in Supplementary Fig. 4c. The mechanical quality factor and frequency shift are directly extracted from the Lorentzian fit of this curve. A disk without pedestal is considered and the substrate is also removed in order to avoid spurious interferences that would complicate interpretations. As apparent in Supplementary Fig. 4d, pressure waves propagate far away from the disk, in contrast to the viscous regime. Note that waves propagate not only in the radial direction but in the z direction as well. A careful study showed us

that the z-propagation also results from interference effects produced by the whole disk, and cannot be solely attributed to the z-displacement of the disk's top and bottom surfaces analyzed in the previous section S2.

Effect of the presence of the waveguide

The presence of the waveguide modifies the liquid mechanical damping in a manner that can be neglected at the level of the present report. In the viscous regime, the boundary layer thickness is typically smaller than the disk/guide gap distance such that the damping is unaffected by the guide. In the acoustic regime, interference patterns can be modified by the presence of the guide but this does not lead to appreciable change in the amount of damping, as checked by 3D simulations. The reason is that the gap between the disk and the guide defines a volume that is small compared to the total volume where the damping takes place. For a disk-guide gap distance evolving between 350 and 500 nm, as employed in the reported experiments, 3D FEM simulation on a disk of radius 1 μm, thickness 320 nm, immersed in water, show that the variations in mechanical Q induced by the presence of the guide are below 5%, while the variations in the mechanical frequency are below 1 %.

4. Analytical theory of the fluid-disk interaction

As stated in the main text, the analytical models we develop in this work to study the fluid-disk interaction build upon the method of decomposing a vibrating structure in elementary pieces of virtual vibrating spheres. Each virtual sphere interacts with the fluid, and we then sum the contribution of all pieces[6,7]. The underlying idea is that the problem of a sphere with its center of mass vibrating harmonically along one direction in a viscoelastic liquid admits an exact hydrodynamic solution, formulated by Oestreicher[8], which can be handled with reasonable effort both in the viscous and acoustic regimes.

From now on we assume that a sphere, with radius noted *a*, is moving along an axis noted x, implying that the displacement of any point of the sphere is simply expressed as $\boldsymbol{u} = \boldsymbol{u_0 e^{i\omega t} x}$. In his paper, Oestreicher[8] solved for the complete velocity field in the fluid in this case, and obtained the force per unit surface *p* exerted by the fluid at any point of the sphere, after projection onto the sphere's vibration direction. Hence *p* is a scalar. An important feature of our model is to take into account the different kinds of motion (longitudinal or shear) involved at the surfaces of the disk resonator. In order to do so formally, we consider two specific points on the sphere that we associate to the two kinds of motion. Firstly, the point A whose normal vector is parallel to the velocity vector (also identified by the coordinate x=a) is associated to a longitudinal motion (the l subscript will refer to longitudinal hereafter), in which the disk surface harmonically pushes the fluid. Secondly, any point B (located on the equatorial line identified by the coordinate x=0) whose normal vector is orthogonal to the velocity vector is associated to a shear motion (the s subscript will refer to shear motion hereafter) of the disk with respect to the fluid.

Note that when the disk is vibrating radially, the sidewall pushes the fluid (longitudinal motion), while the top and bottom surfaces experience a shear motion relative to the fluid. Concomitantly, as discussed in section S2, the disk also expands and contracts in the z-direction by virtue of the Poisson ratio. As a result, the top and bottom surfaces of the disk also push the fluid (longitudinal motion), while the sidewall acquires a shear motion component with respect to the fluid. In a RBM, this out-of-plane z-motion is much smaller than the radial motion; nevertheless we will see in the following that it needs to be accounted for in order to gain an optimal quantitative understanding.

In ref. 8, a viscoelastic fluid is characterized by its density $\boldsymbol{\rho}$, its complex viscosity $\boldsymbol{\mu_f = \mu_1 + i\omega\mu_2}$ where $\boldsymbol{\mu_1}$ is the shear elasticity and $\boldsymbol{\mu_2}$ the usual dynamic viscosity, and its complex elasticity modulus $\boldsymbol{K_f = K_1 + i\omega K_2}$, where $\boldsymbol{K_1}$ is the coefficient of volume compressibility and $\boldsymbol{K_2}$ the coefficient of

volume viscosity. In the following we restrict the problem to two special cases of interest, the incompressible viscous medium and the acoustic medium. In both cases, the shear elasticity is considered equal to zero therefore $\boldsymbol{\mu_f = i\omega\mu_2}$ and we adopt the standard notation $\boldsymbol{\mu_2 = \mu}$. At the same time, for the incompressible viscous case $\boldsymbol{K_1}$ is considered infinite, while in the acoustic case $\boldsymbol{K_2}$ is equal to zero and the speed of sound in the fluid is simply $\boldsymbol{c = \sqrt{K_1/\rho}}$.

4.1. Incompressible viscous medium

An incompressible viscous fluid is defined as a fluid with infinite coefficient of volume compressibility ($\boldsymbol{K_1 = \infty}$), which implies infinite speed of sound. By imposing this condition and following derivations of ref 8, the viscous force per unit surface p^v at points A and B (corresponding to longitudinal and shear motion) is given by:

$$\boldsymbol{p_l^v = -(\frac{5\mu}{2a}\mu + \frac{5}{4}\sqrt{2\rho\mu\omega} + \frac{5}{4}\sqrt{2\rho\mu\omega}i + \frac{1}{2a}\rho\omega i)i\omega u_0 e^{i\omega t}} \quad \text{(S3)}$$

$$\boldsymbol{p_s^v = -(\frac{\mu}{a} + \frac{1}{2}\sqrt{2\rho\mu\omega} + \frac{1}{2}\sqrt{2\rho\mu\omega}i)i\omega u_0 e^{i\omega t}} \quad \text{(S4)}$$

where *a* is the radius of the sphere and where the subscripts *l* and *s* refer respectively to longitudinal and shear motion. This expression can be re-organized as the sum of 3 terms proportional to the velocity, acceleration and displacement of the sphere:

$$\boldsymbol{p = -\alpha\dot{u} - \beta\ddot{u} - \gamma u} \quad \text{(S5)}$$

If we consider the equation of motion of an harmonic oscillator $\boldsymbol{m\ddot{x} + kx = F}$, where $\boldsymbol{m}$ is the mass, $\boldsymbol{k}$ the stiffness and F an applied force, the first term on the right hand side of equation S5 becomes associated to

a velocity-dependent damping force, the second to an additional mass decreasing the mechanical frequency and the third to an added spring that increases the frequency. The fluidic damping, the mass and stiffness added by the fluid are obtained by integrating these 3 contributions over the entire resonator surface. From equations S3 and S4 we directly obtain $\boldsymbol{\gamma_l^v = \gamma_s^v = 0}$ and for the other terms:

$$\boldsymbol{\alpha_l^v = \frac{5\mu}{2a} + \frac{5}{4}\sqrt{2\rho\mu\omega}} \qquad \boldsymbol{\beta_l^v = \frac{1}{2}\rho a + \frac{5}{4}\sqrt{2\rho\mu/\omega}} \tag{S6}$$

$$\boldsymbol{\alpha_s^v = \frac{\mu}{a} + \frac{1}{2}\sqrt{2\rho\mu\omega}} \qquad \boldsymbol{\beta_s^v = \frac{1}{2}\sqrt{2\rho\mu/\omega}} \tag{S7}$$

$\boldsymbol{\alpha^v}$ is similar for both longitudinal and shear motion, only differing by the constant 5/2. $\boldsymbol{\alpha^v}$ contains two terms, one linearly dependent on the viscosity and the other proportional to the square root of the density, viscosity and angular frequency of oscillation. Regarding the inertial force $\boldsymbol{\beta^v}$, it contains two terms for the longitudinal motion and only one for the shear. The common term is proportional to the square root of density times viscosity and is again 5/2 times larger for longitudinal motion compared to shear motion. In addition, the second term, which is absent in the shear motion, is independent of the fluid viscosity and only scales with density. Some terms in equations S6 and S7 depend on the sphere radius *a*, showing that the choice of the virtual sphere size should impact the model results. Intuitively, the sphere size should be related to some typical dimension of the device moving in the fluid, and may hence differ for each considered surface of the disk. Here, for the motion of the disk's sidewall we choose the sphere's radius equal to the disk's thickness $\boldsymbol{a = H}$, while $\boldsymbol{a = R}$ is taken for the motion of top and bottom surfaces. This choice is validated by the solid agreement obtained with FEM simulations.

The mechanical quality factor $\boldsymbol{Q_m}$ can be derived through the equation $\boldsymbol{Q_m = 2\pi\frac{E}{\Delta E}}$ where E is the mechanical energy stored in the resonator and $\boldsymbol{\Delta E}$ is the energy dissipated per oscillation cycle. We consider an harmonic displacement field for the disk $\boldsymbol{\Psi = \Psi(r,\theta,z)e^{i\omega t}}$. For the RBM motion, we have

considered above the radial and the out-of-plane z-displacement, hence the total displacement at any point of the disk is expressed as $\boldsymbol{\Psi(r,z) = \Psi_r(r)r + \Psi_z(r,z)z}$ and the energy stored in the disk is the sum of both radial and out-of-plane contributions $\boldsymbol{E = \frac{1}{2}\iiint_V \rho_s \dot{\Psi}^2 dV = \frac{1}{2}\iiint_V \rho_s \dot{\Psi}_r^2 dV + \frac{1}{2}\iiint_V \rho_s \dot{\Psi}_z^2 dV}$. The energy lost per cycle of oscillation due to the interaction fluid has the general form $\boldsymbol{\Delta E = \int_0^T \iint_S \alpha \Psi^2 dS dt}$. Summing the contributions of both top and bottom surfaces and disk sidewall for the two kind of motions considered (longitudinal and shear), we finally obtain:

$$\boldsymbol{Q_{viscous} = \frac{\rho_s \omega \left[H \int_0^R \Psi_r^2 r\, dr + \int_{-H/2}^{H/2} \left(\int_0^R \Psi_z^2 r\, dr \right) dz \right]}{RH\alpha_l^v \Psi_r^2|_{r=R} + 2\alpha_s^v \int_0^R \Psi_r^2 r\, dr + R\alpha_s^v \int_{-H/2}^{H/2} \Psi_z^2|_{r=R}\, dz + 2\alpha_l^v \int_0^R \Psi_z^2|_{z=H/2} r\, dr}} \quad \text{(S8)}$$

Note that this expression is valid for any employed elastic material for the disk.

We proceed in a similar manner in order to derive the mechanical frequency shift and obtain the analog formula

$$\boldsymbol{\frac{\Delta f}{f} = \frac{RH\beta_l^v \Psi_r^2|_{r=R} + 2\beta_s^v \int_0^R \Psi_r^2 r\, dr + R\beta_s^v \int_{-H/2}^{H/2} \Psi_z^2|_{r=R}\, dt + 2\beta_l^v \int_0^R \Psi_z^2|_{t=H/2} r\, dr}{\rho_s \left[H \int_0^R \Psi_r^2 r\, dr + \int_{-H/2}^{H/2} (\int_0^R \Psi_z^2 r\, dr)\, dt \right]}} \quad \text{(S9)}$$

At this stage, we inject equations S6 and S7 into equations S8 and S9 and use the Poisson ratio of GaAs in order to fix the frequency parameter λ and the associated analytical spatial profile of the RBM. Substituting the radius of the sphere *a* as previously discussed, the expressions for the viscous quality factor and frequency shift read

$$\boldsymbol{Q_{viscous} = \frac{(HR^2 + 0.1 \cdot H^3)\rho_s}{(8.36 \cdot R + 1.53 \cdot H^2/R)\frac{\mu}{\omega} + (4.50 \cdot HR + 1.41 \cdot R^2 + 0.01 \cdot H^3/R + 1.07 \cdot H^2)\sqrt{\frac{\rho\mu}{\omega}}}} \quad \text{(S10)}$$

$$\Delta f/f = -\frac{0.787 \cdot RH^2\rho + \left(70.71 \cdot R^2 + 224.9 \cdot HR + 53.3 \cdot H^2 + 0.7 \cdot \frac{H^3}{R}\right)\sqrt{\frac{\rho\mu}{\omega}}}{(HR^2 + 0.1 \cdot H^3)\rho_s} \quad \text{(S11)}$$

Note that equations S10 and S11 are still valid for a material with a Poisson ratio close to that of GaAs, like silicon. Obviously all the terms appearing at the numerator and denominator of these expressions have different weights that depend on the frequency regime, on the dimensions of the disk, and on the fluid properties. For a large disk with $R>3H$ the energy and added mass due to the z-displacement is negligible (<2 %). If we now inject the specific values of the Young's modulus and density of GaAs, the expressions transform into semi-numerical forms

$$Q_{viscous} = \frac{1.624 \cdot 10^{11} HR^2}{\mu(29{,}407 \cdot R^2 + 5{,}377 \cdot H^2) + 65.9\left(22{,}373 \cdot HR^2 + 7{,}034 \cdot R^3 + 5{,}305 \cdot H^2 R\right)\sqrt{\frac{\rho\mu}{R}}} \quad \text{(S12)}$$

$$\Delta f/f = -\frac{1.2745 \cdot H^2 R\rho + (1.23 \cdot 10^{-2} R^2 + 3.91 \cdot 10^{-2} HR + 0.93 \cdot 10^{-2} H^2)\sqrt{R\rho\mu}}{8{,}607 \cdot HR^2} \quad \text{(S13)}$$

where numbers are now to be taken in SI units to obtain the correct physical dimensions of all terms. For the parameters of liquid viscosity and density used in our experiments, the dissipative contribution proportional to the viscosity can also be neglected and the dominating dissipative term is the one proportional to $\sqrt{\rho\omega\mu}$. The z-displacement of the top and bottom surfaces accounts for example for 5% of the energy losses when $R=3H$, and cannot be always neglected. We will however omit these terms to converge towards approximate expressions. A simplified expression for the viscous quality factor is finally

$$Q_{viscous} = \frac{3.34 \cdot 10^5}{3.18 \cdot R^{-1/2} + R^{1/2}/H}(\rho\mu)^{-1/2} \quad \text{(S14)}$$

For what concerns the frequency shifts, the main contribution is generally the first numerator term proportional to the density, however the second term also becomes important as the viscosity rises. More precisely, the z-displacement of the top and bottom surfaces has an impact on the term proportional to the density, but barely any impact on the term proportional to $\sqrt{\boldsymbol{\rho}\mu}$. This finally simplifies the numerical form of the analytical formula to (in SI)

$$\Delta \boldsymbol{f}/\boldsymbol{f} = -\left[(\mathbf{1.481}\cdot\mathbf{10^{-4}})\boldsymbol{\rho}\frac{\boldsymbol{H}}{\boldsymbol{R}} + \left(\frac{\mathbf{4.543}\cdot\mathbf{10^{-6}}}{\boldsymbol{R}} + \frac{\mathbf{1.429}\cdot\mathbf{10^{-6}}}{\boldsymbol{H}}\right)\sqrt{\boldsymbol{R\rho\mu}}\right] \quad \text{(S15)}$$

Note again that in equations S14 and S15, numbers must be taken in SI units to obtain the correct physical dimensions of all terms.

4.2. Perfect acoustic medium

The acoustic regime corresponds to a finite volume compressibility and zero viscosity, be it shear or longitudinal. We start by following the same steps as for the viscous case, and decompose the problem into elementary pieces of spheres. Imposing acoustic conditions on the derivations of ref 8, we obtain the acoustic force per unit surface p^a exerted by the fluid on the sphere, once projected onto the sphere's vibration direction, and considered for both longitudinal and shear motion

$$\boldsymbol{p_l^a} = -\frac{\boldsymbol{a^4\omega^4 c\rho + (2a\omega c^4 + a^3\omega^3 c^2)\rho i}}{\mathbf{4c^4} + \boldsymbol{a^4\omega^4}}\boldsymbol{i\omega u_0 e^{i\omega t}} \quad \text{(S16)}$$

$$\boldsymbol{p_s^a} = \mathbf{0} \quad \text{(S17)}$$

Importantly, this acoustic force amounts to zero for shear motion $\boldsymbol{\alpha_s^a = \beta_s^a = \gamma_s^a = 0}$. As a consequence, only the radial movement at the sidewall and the out-of-plane motion of the top and bottom surfaces shall be considered. The corresponding expressions for $\boldsymbol{\alpha}$, $\boldsymbol{\beta}$ and $\boldsymbol{\gamma}$ are

$$\boldsymbol{\alpha_l^a = \frac{a^4\omega^4 c}{4c^4+a^4\omega^4}\rho} \qquad \boldsymbol{\beta_l^a = \frac{2ac^4}{4c^4+a^4\omega^4}\rho} \qquad \boldsymbol{\gamma_l^a = \frac{a^3\omega^4 c^2}{4c^4+a^4\omega^4}\rho} \tag{S18}$$

All the terms have a direct proportionality to density and have a maximum at a speed of sound that depends on the frequency and the sphere's radius a. By integrating over the whole surface of the disk we obtain for the acoustic quality factor

$$\boldsymbol{Q_{acoustic} = \frac{\rho_s \omega H \int_0^R \Psi_r^2 r\, dr + \int_{-H/2}^{H/2}\left(\int_0^R \Psi_z^2 r\, dr\right) dz}{RH\alpha_l^a \Psi_r^2|_{r=R} + 2\alpha_l^a \int_0^R \Psi_z^2|_{z=H/2} r\, dr}} \tag{S19}$$

while the frequency shift is expressed as

$$\boldsymbol{\frac{\Delta f}{f} = \frac{RH\gamma_l^a \Psi_r^2|_{r=R} + 2\gamma_l^a \int_0^R \Psi_z^2|_{t=H/2} r\, dr}{2\omega^2\left(H\rho_s \int_0^R \Psi_r^2 r\, dr + 2\pi\rho_s \int_{-H/2}^{H/2}(\int_0^R \Psi_z^2 r\, dr)\, dz\right)} - \frac{RH\beta_l^a \Psi_r^2|_{r=R} + 2\beta_l^a \int_0^R \Psi_z^2|_{t=H/2} r\, dr}{2H\rho_s \int_0^R \Psi_r^2 r\, dr + 4\pi\rho_s \int_{-H/2}^{H/2}(\int_0^R \Psi_z^2 r\, dr)\, dz}} \tag{S20}$$

As for the viscous case, we make use of S18 in S19 and S20 and consider the Poisson ratio of GaAs to fix the mode profile. As previously, we chose the sphere radius *a* to be equal to the disk's thickness $\boldsymbol{a = H}$ for the disk's sidewall, while $\boldsymbol{a = R}$ is taken for the motion of top and bottom surfaces, finally we obtain

$$\boldsymbol{Q_{acoustic}^{-1} = \frac{H}{R}\frac{\rho}{\rho_s}\left[0.603\,\frac{\left(\frac{\lambda}{\sqrt{1-\nu^2}}\frac{c_S}{c}\right)^3}{4+\left(\frac{\lambda}{\sqrt{1-\nu^2}}\frac{c_S}{c}\right)^4} + 2.545\,\frac{\left(\frac{\lambda}{\sqrt{1-\nu^2}}\frac{c_S H}{c\, R}\right)^3}{4+\left(\frac{\lambda}{\sqrt{1-\nu^2}}\frac{c_S H}{c\, R}\right)^4}\right] \Big/ \left(1 + 0.1 \cdot H^2/R^2\right)} \tag{S21}$$

$$\left(\frac{\Delta f}{f}\right)_{acoustic} = \frac{\frac{\rho}{\rho_S}\frac{H}{R}\left[\left(\frac{0.302}{4+\left(\frac{\lambda}{\sqrt{1-\nu^2}}\frac{c_S}{c}\right)^4}+\left(\frac{H}{R}\right)^2\frac{1.272}{4+\left(\frac{\lambda}{\sqrt{1-\nu^2}}\frac{c_S H}{c R}\right)^4}\right)\left(\frac{\lambda}{\sqrt{1-\nu^2}}\frac{c_S}{c}\right)^2-\left(\frac{0.603}{4+\left(\frac{\lambda}{\sqrt{1-\nu^2}}\frac{c_S}{c}\right)^4}+\frac{2.545}{4+\left(\frac{\lambda}{\sqrt{1-\nu^2}}\frac{c_S H}{c R}\right)^4}\right)\right]}{1+0.1\cdot H^2/R^2} \quad \text{(S22)}$$

These expressions enable us to identify some meaningful analytical blocks of importance to describe acoustic interactions. However, in contrast to the viscous regime, the propagation of acoustic waves can lead to complex interferences in the fluid that would not be correctly retrieved by simply summing up the acoustic emission of isolated pieces of spheres. When comparing the output of a sphere approach with FEM, we indeed observe that several important trends are correctly reproduced while some others are not, notably the evolution of Q as a function of speed of sound. Quantitative agreement is also less satisfying than in the viscous regime. To advance further, we adopted the strategy of building empirical formulas based on the identified analytical building blocks. By systematic cross-checks with FEM results, we finally obtain the formulas shown in the main text

$$Q^{-1}_{acoustic} = \frac{H}{R}\frac{\rho}{\rho_S}\left[1.92\frac{\left(\frac{1}{2}\frac{\lambda}{\sqrt{1-\nu^2}}\frac{c_S}{c}\right)^3}{4+\left(\frac{1}{2}\frac{\lambda}{\sqrt{1-\nu^2}}\frac{c_S}{c}\right)^4}+1.05\left(\frac{H}{R}\right)^{-1/2}\frac{\left(\frac{3}{4}\frac{\lambda}{\sqrt{1-\nu^2}}\frac{c_S H}{c R}\right)^3}{4+\left(\frac{3}{4}\frac{\lambda}{\sqrt{1-\nu^2}}\frac{c_S H}{c R}\right)^4}\right] = f\left(\frac{H}{R},\frac{\rho}{\rho_S},\frac{c_S}{c},\nu\right) \quad \text{(S22)}$$

$$\left(\frac{\Delta f}{f}\right)_{acoustic} = -0.954\frac{H}{R}\frac{\rho}{\rho_S}\left[\frac{1}{4+\left(\frac{1}{4}\frac{\lambda}{\sqrt{1-\nu^2}}\frac{c_S}{c}\right)^4}+\frac{2.4}{4+\left(\frac{3}{5}\frac{\lambda}{\sqrt{1-\nu^2}}\frac{c_S H}{c R}\right)^4}\right] = g\left(\frac{H}{R},\frac{\rho}{\rho_S},\frac{c_S}{c},\nu\right) \quad \text{(S23)}$$

5. Additional informations on analytical models of fluid-disk interaction

Because of space constraints, only a part of the tests carried-out on our analytical models is shown in the main text. Here we show additional FEM simulations to further demonstrate their validity, focusing on

dependence of the mechanical quality factor and frequency shift on liquid properties. The results are summarized in Supplementary Fig. 5 and 6.

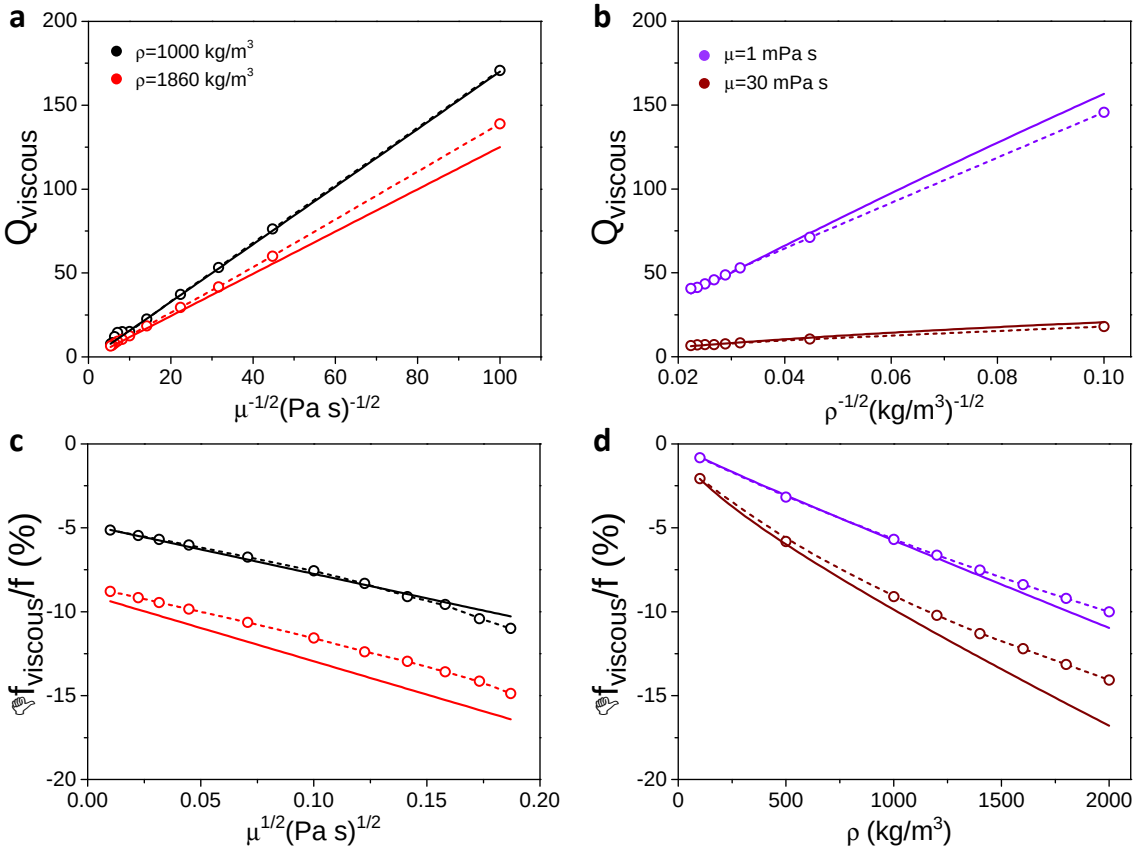

Supplementary Figure 5: Viscous models as a function of fluid properties. The novel analytical model (solid lines) is systematically confronted to FEM results (open circles with dashed lines) for a disk radius and thickness of 1 μm and 320 nm respectively. **a,** Mechanical quality factor as a function of the liquid viscosity for two different liquid densities ρ=1000 kg/m^3 (black) and ρ =1860 kg/m^3 (red). **b,** Mechanical quality factor as a function of the liquid density for two different viscosities: μ=1 mPa s (violet) and μ =30 mPa s (wine). **c**, **d,** The corresponding relative mechanical shift Δf/f as a function of the same parameters.

Supplementary Fig. 5a, b show the viscous quality factor as a function of the density and the viscosity of the fluid, with the exact behavior expected from the analytical expression S14. The mechanical frequency

shift shown in Supplementary Fig. 5c, d displays a strong dependence on the density and viscosity of the fluid, as underlined by equation S15.

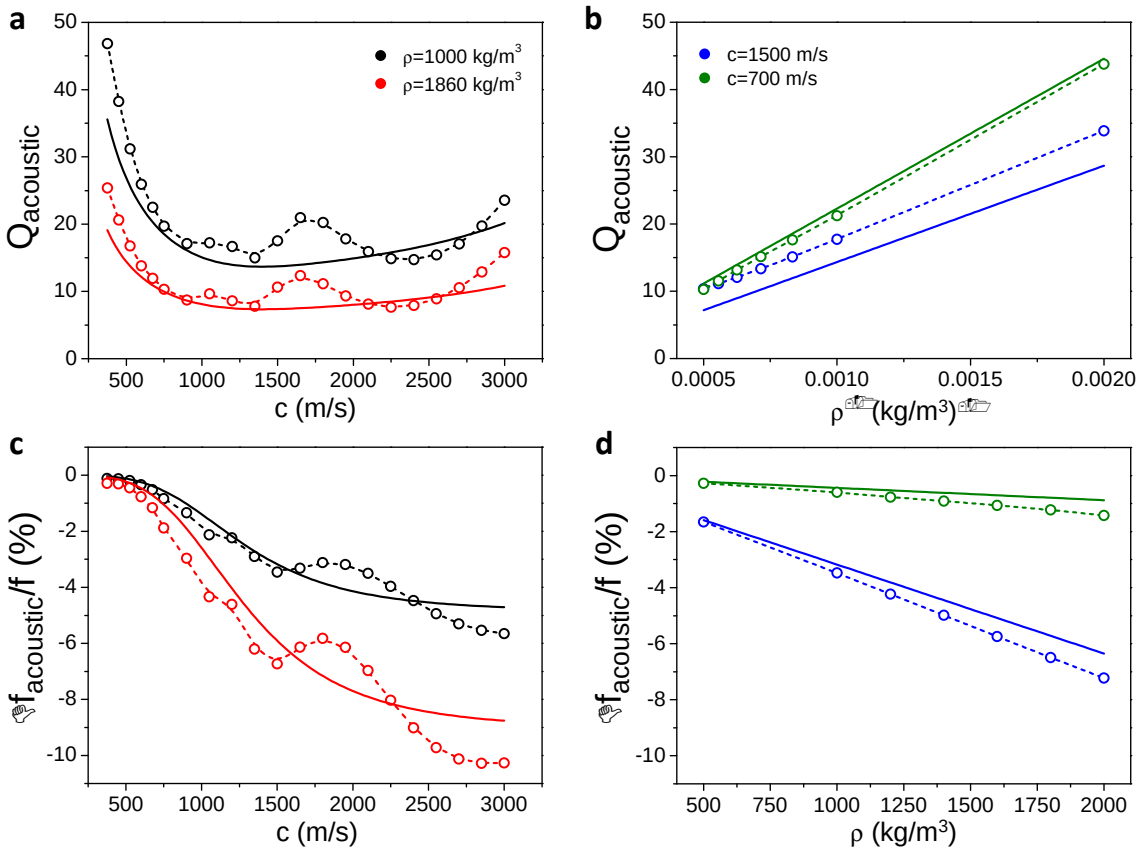

Supplementary Figure S6: Acoustic models as a function of fluid properties. The novel analytical model (solid lines) is systematically confronted to FEM results (open circles with dashed lines) for R=1 µm and H=320 nm. **a,** Mechanical quality factor as a function of the liquid's speed of sound for two different densities ρ=1000 kg/m^3 (black) and ρ =1860 kg/m^3 (red). **b,** Mechanical quality factor as a function of the liquid density for two different fluid speeds of sound c=1500 m/ s (blue) and c=700 m/ s (green). **c**, **d,** The corresponding relative mechanical shift Δf/f for the same parameters.

Supplementary Fig. 6 focuses on the acoustic model. In Supplementary Fig. 6a and c, FEM results show a complex dependence of the mechanical quality factor and frequency shift as a function of the liquid's speed of sound. The apparent oscillations are likely due to pressure waves interferences. Our analytical

model reproduces the overall FEM results without the details of these interferences. The dependence with the density parameter is simpler, as also clear from expressions S22 and S23. Supplementary Fig. 6b and d show a solid agreement between analytical and numerical models as a function of density.

References

1 Vogel, M., Mooser, C., Karrai, K. & Warburton, R. J. Optically tunable mechanics of microlevers. *Appl. Phys. Lett.* **83**, 1337-1339 (2003).

2 Carmon, T., Yang, L. & Vahala, K. Dynamical thermal behavior and thermal self-stability of microcavities. *Opt. Express* **12**, 4742-4750 (2004).

3 Ding, L. *et al.* Wavelength-sized GaAs optomechanical resonators with gigahertz frequency. *Appl. Phys. Lett.* **98**, 113108 (2011).

4 Love, A. E. H. *A Treatise On The Mathematical Theory Of Elasticity*. (Cambridge University Press, Cambridge, 1906).

5 Onoe, M. Contour Vibrations of Isotropic Circular Plates. *J. Acoust. Soc. Am.* **28**, 1158-1162 (1956).

6 Hosaka, H., Itao, K. & Kuroda, S. Damping characteristics of beam-shaped micro-oscillators. *Sens. Actuators, A* **49**, 87-95 (1995).

7 Parrain, D. *et al.* Damping of optomechanical disks resonators vibrating in air. *Appl. Phys. Lett.* **100**, 242105 (2012).

8 Oestreicher, H. L. Field and impedance of an oscillating sphere in a viscoelastic medium with an application to biophysics. *J. Acoust. Soc. Am.* **23**, 707-714 (1951).